Available online at www.sciencedirect.com
ScienceDirect
Aerosol Science 38 (2007) 728–746
Journal of Aerosol Science
www.elsevier.com/locate/jaerosci

Particle formation in spray drying

Reinhard Vehring[a,*], Willard R. Foss[b,1], David Lechuga-Ballesteros[b]

[a] *MedImmune, Inc., 319 North Bernardo Ave., Mountain View, CA 94043, USA*
[b] *Nektar Therapeutics, 150 Industrial Rd., San Carlos, CA 94070, USA*

Received 24 January 2007; received in revised form 25 April 2007; accepted 30 April 2007

Abstract

Theoretical and experimental investigations of the particle formation process during spray drying are presented. A novel experimental method allows observation of individual, free flowing droplets during drying in a laminar gas flow and subsequent analysis of the resulting monodisperse, monomorphic dry particles. A second method combines a vibrating orifice generator and a bench top spray drier, which allows production and sampling of monodisperse particles at different drying stages. The experimental results are compared to a full numerical model and a simplified analytical model. Two dimensionless parameters are identified that influence particle formation: the Peclet number, which is the ratio of the diffusion coefficient of the solute and the evaporation rate, and the initial saturation of the excipients. In an application example, particle design is shown to improve the aerosol properties of powders intended for pulmonary drug delivery.

Keywords: Particle engineering; Structured microparticles; Droplet evaporation; Drying kinetics

1. Introduction

Spray drying is a widely used manufacturing process which uses the aerosol phase to dry particles. The technology has been applied in many areas, including the food, pharmaceutical, ceramic, polymer, and chemical industries (Masters, 1972). Spray drying is a well-established technique that has been used for over a century but it remains an active field of innovation, driven by the ever increasing demand for more sophisticated particles.

In the pharmaceutical industry spray drying is used to manufacture particles that form the basis for dry dosage forms for parenteral, nasal, or pulmonary delivery, and are administered as suspensions, powders, or aerosols. These particles must be able to stabilize the active pharmaceutical ingredient and provide physical stability for the dosage form on storage. They must have adequate powder flow properties and dispersibility, and, in the case of respiratory delivery, suitable aerodynamic properties. In recent years, particle engineering has been used to design complex particles which meet these demands. Hollow, low density particles with controlled surface morphology, particles with functional layers, or particles comprising smaller subunits such as nanoparticles or defined voids, have been introduced (Edwards et al., 2002; Kuo & Lechuga-Ballesteros, 2003; Platz, Patton, Foster, & Eljamal, 2002; Weers, Schutt, Dellamary, Tarara, & Kabalnov, 2001). Because of the complexity of these particles, a sound understanding of the particle formation

* Corresponding author. Tel.: +1 650 603 2579; fax: +1 650 603 3579.
E-mail address: vehringr@medimmune.com (R. Vehring).
[1] Current address: Amgen, Inc., One Amgen Center Dr., Thousand Oaks, CA 91320, USA.

0021-8502/$ - see front matter © 2007 Elsevier Ltd. All rights reserved.
doi:10.1016/j.jaerosci.2007.04.005

process is necessary for successful particle engineering. This motivates further research into the physical and chemical mechanisms that control the drying and particle formation process in the aerosol phase. Several experimental techniques for the investigation of the drying process have been introduced in the literature. Many of these techniques are used to study an idealized system, comprised of suspended or levitated individual droplets or moving chains of similar droplets.

An overview of studies on droplets suspended from thin filaments can be found in recent reports. Lin and Gentry (2003) observed the particle formation process of millimeter-sized droplets suspended from a filament, and investigated particle density and morphology as a function of latent heat of crystallization, solubility, and drying rate. The technique was further refined by Lin and Chen (2004) and Chen and Lin (2004) and used to monitor the drying process of milk droplets. Drops suspended from filaments have been used frequently to study the morphology of dried particles (El-Sayed, Wallack, & King, 1990; Lin & Chen, 2002; Sunkel & King, 1993; Walton & Mumford, 1999), beginning with Charlesworth and Marshall (1960), who studied crust formation in evaporating drops. However, the use of a filament to suspend droplets has limitations. Most frequently mentioned are the need to work with relatively large droplets in the millimeter diameter range, and deviation from normal heat transfer because of heat conduction between droplet and filament.

Tsapis et al. (2005) and Sugiyama, Larsen, Kim, and Weitz (2006) have levitated droplets using the Leidenfrost phenomenon on a concave hot plate. This technique was successfully used to study shell buckling during particle formation. A drawback of this approach is that the flow field and temperature field in the vicinity of the droplet are different from those of a free flowing droplet in a spray dryer.

A chain of monodisperse free falling droplets has been used by several groups to study heat and mass transfer, drying, and particle formation processes. El Golli, Bricard, Turpin, and Treiner (1974) measured salt droplet evaporation and compared their results with a theoretical model. Alexander and King (1985) and El-Sayed et al. (1990) used a similar technique to study the effect of drying rates on particle formation. Greenwald and King (1982) used a droplet chain to study the formation of internal voids in particles. Wallack, El-Sayed, and King (1990) compared measured evaporation rates with a numerical model, achieving fairly good agreement. The droplet generators used in these studies produce a chain of closely spaced droplets, which leads to droplet–droplet interactions in processes that are limited by gas phase transport processes. A review of single drop and droplet chain techniques is given by Adhikari, Howes, Bhandari, and Truong (2000). None of the reviewed studies investigated droplets smaller than 170 μm.

Realistically sized droplets have mainly been studied in small scale spray dryers. Many aspects of the drying process have been investigated. Tsapis, Bennett, Jackson, Weitz, and Edwards (2002) pointed to the importance of the ratio between evaporation rate and diffusional motion of the solutes and used the concept of the Peclet number to explain the low density of particles spray dried from suspensions of nanoparticles. In a study on polymer nanoparticles, Raula, Eerikäinen, and Kauppinen (2004) showed that solubility and precipitation kinetics of the solutes play an important role in particle formation. Maa, Costantino, Nguyen, and Hsu (1997) studied the morphology and solid state properties of spray dried protein-sugar particles and found that crystallinity may be influenced by the evaporation rate. Elversson and Millqvist-Fureby (2005) demonstrated that feed concentration and solubility affect particle density. Fäldt and Bergenståhl (1994) studied the surface composition of spray dried particles and found that the surface tension of the components affect the composition of the air–water interface of the drying droplet which in turn determines the composition of the surface layer of the dry particles.

This paper employs a combination of experimental tools, a full numerical model, and a simplified analytical model to study the evaporation and particle formation processes. The experimental tools are an improved droplet chain technique that solves the issue of droplet–droplet interactions, and a modified spray dryer that produces controlled monodisperse particles. The theoretical models are used to derive dimensionless numbers that can be used to describe the aerosol particle formation process and identify the main controlling parameters.

2. Theory

2.1. Analytical

The evaporation of a solution droplet during spray drying can be described as a coupled heat and mass transport problem. The difference between the vapor pressure of the solvents and their partial pressure in the gas phase is the driving force of the drying process. The rate of evaporation is determined by a balance of the energy flux required for the enthalpy of vaporization and the energy flux transported to the surface of the droplet. The latter can be provided

from the gas phase and from the heat capacity of the droplet through droplet cooling. The evaporation rate determines the surface recession rate of the droplet. The receding droplet surface causes a diffusional flux of the solutes away from the surface towards the center of the droplet. In the absence of internal convection, the distribution of the chemical components in an evaporating droplet is described by the non-linear diffusion equation which becomes Fick's second law of diffusion if no interactions between the solutes and constant diffusion coefficients are assumed. In the case of radial symmetry, using the normalized radial coordinate, $R = r/r_s$, this equation can be written as

$$\frac{\partial c_i}{\partial t} = \frac{D_i}{r_s^2}\left(\frac{\partial^2 c_i}{\partial R^2} + \frac{2\partial c_i}{R\partial R}\right) + \frac{R\partial c_i \partial r_s}{r_s \partial R \partial t}, \tag{1}$$

where c_i denotes the concentration of solute i and D_i the diffusion coefficient of solute i in the liquid phase. r_s is the droplet radius.

Eq. (1) has an analytical solution under the steady-state condition:

$$r_s \frac{\partial r_s}{\partial t} = const. \tag{2}$$

The steady-state evaporation of a water droplet of diameter, d, is proportional to the surface area of the droplet. The evaporation rate, κ, is defined as

$$d^2(t) = d_0^2 - \kappa t. \tag{3}$$

A constant evaporation rate fulfills condition (2), because

$$\frac{\partial d^2}{\partial t} = -\kappa = 8 r_s \frac{\partial r_s}{\partial t}. \tag{4}$$

The solution to Eq. (1) under the assumption of constant evaporation is given by Leong (1987):

$$c_i = c_{c,i} \exp\left(-\frac{r_s \partial r_s}{2 D_i \partial t} R^2\right). \tag{5}$$

Eq. (5) expresses the concentration, c, as a function of the concentration at the center of the droplet, c_c. It is more useful to express the concentration as a function of the average concentration, c_m, in the droplet, because it can be calculated from the initial conditions at any time in the droplet history as long as the evaporation rate is constant using a simple mass balance in combination with Eq. (3). Hence, after Eq. (5) is integrated over the volume of the sphere to introduce the average concentration, rearrangement yields

$$c_i = c_{m,i} \frac{\exp(Pe_i R^2/2)}{3\int_0^1 R^2 \exp(Pe_i R^2/2)\,\mathrm{d}R}. \tag{6}$$

Here the dimensionless Peclet number, Pe, has been introduced to simplify the equation:

$$Pe_i = -\frac{r_s \partial r_s}{D_i \partial t} = \frac{\kappa}{8 D_i}. \tag{7}$$

For $R = 1$ we find the surface concentration

$$c_{s,i} = \frac{c_{m,i}}{3\beta_i} \exp\left(\frac{Pe_i}{2}\right) \quad \text{with } \beta_i = \int_0^1 R^2 \exp\left(\frac{Pe_i}{2} R^2\right) \mathrm{d}R. \tag{8}$$

β must be integrated numerically for each Pe number to obtain the exact solution. Alternatively, an approximate expression for the surface enrichment, E_i,

$$E_i = \frac{c_{s,i}}{c_{m,i}} = 1 + \frac{Pe_i}{5} + \frac{Pe_i^2}{100} - \frac{Pe_i^3}{4000} \tag{9}$$

can be used with an accuracy of $\pm 1\%$ for $Pe < 20$.

This constant evaporation model assumes that during most of the evaporation the gas temperature and thus the droplet temperature are constant. It does not account for the non-stationary evaporation at the beginning of the evaporation process, where the droplet temperature rapidly changes, nor does it account for any changes in the evaporation rate immediately prior to solidification of the particles. In general, the diffusion coefficients depend on the concentration of the solutes and change significantly during the drying process, especially when solute concentrations reach supersaturation or the liquid phase viscosity increases prior to solidification. This simplification prevents the application of the analytical model during the solidification of the particles.

2.2. Numerical

The analytical model cannot correctly describe the non-stationary phases of the evaporation, which are the initial temperature change of the droplet as it approaches the quasi-steady equilibrium of the constant evaporation rate period, and more importantly, the solidification of the particle during the late stage of the evaporation. These processes must be described by coupled heat and mass transfer equations in the gas and the droplet. Because there is no analytical solution for this set of equations, a numerical treatment becomes necessary.

Many models for single droplet evaporation have been developed, for example in the area of droplet combustion. Reviews were given by Law (1982), Davis (1983), and Kreidenweis, Flagan, and Seinfeld (1987). The model used in this paper was developed for the case of microdroplets with initial diameters on the order of 10 μm dried at moderate gas temperatures, a situation commonly encountered in pharmaceutical processing in the area of pulmonary drug delivery. The droplet Reynolds numbers for these comparatively small droplets are low enough to justify a model that treated the gas phase as quiescent and neglected internal circulation in the droplets. Heat conduction in the liquid phase is fast compared to that in the gas phase and to the mass transport, so at the moderate temperature differences between drying gas and droplet considered here, the droplet temperature may be treated as spatially homogeneous. It was not attempted to model the actual solidification process, because material properties necessary to calculate the stress in partially dried particles could not be found. Hence, momentum conservation was neglected and the system was treated as isobaric. The model accounted for multiple solutes and solvents and allowed multiple volatile components, but did not consider reactions between the components. The gas phase was treated as a mixture of ideal gases. No convection other than the Stefan flow, Newbold and Amundson (1973), in the gas phase and the corresponding term in the liquid phase was considered. Hence, a one-dimensional treatment of the problem in spherical symmetry became possible. The model allowed locally and temporally variable material properties and variable drying gas conditions far away from the droplet. A more detailed description of the governing equations with their boundary conditions is given in Appendix B.

Because the concentration of the solutes close to the surface of the droplet is important for the interpretation of the particle formation process, the computational grid provided increased resolution near the droplet surface and the radial coordinate was non-dimensionalized by the actual droplet radius at each point in the evaporation. Therefore, the relative spatial resolution of the model was maintained throughout the evaporation process independent of droplet size. The differential equations were solved using the backwards Euler method. Newton–Raphson iteration was used to reach convergence. Variable time steps were implemented to deal with parts of the problem where evaporation rates and temperatures change rapidly, for example in the initial phase of the evaporation.

3. Experimental

3.1. Instruments

The droplet chain technique shown in Fig. 1a was an improved version of similar techniques that have been used previously to study heat and mass transfer processes on droplets. These techniques have commonly used a vibrating orifice generator which is capable of producing monodisperse droplets over a large droplet diameter range. However, the droplet spacing in chains produced by a vibrating orifice generator is only on the order of several droplet diameters. This leads to droplet–droplet interactions during the evaporation process, mainly droplet collisions (Anders, Roth, & Frohn, 1992) and an increase of the solvent vapor pressure around the closely spaced droplets (Vehring & Schweiger, 1991), which affects the progression of the evaporation (Devarakonda & Ray, 2003). The generator used in this study was a droplet-on-demand type (modified dispenser head, MD-K-130, Microdrop Technologies, Hamburg, Germany) capable of producing droplets with a diameter larger than 10 μm at variable production frequencies, including single droplet

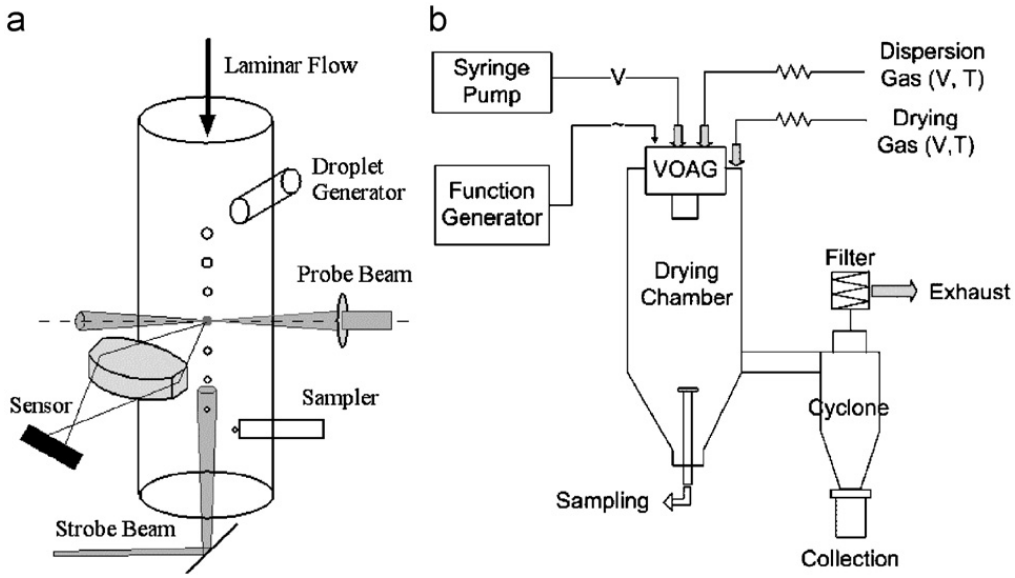

Fig. 1. Experimental techniques: (a) the droplet chain technique; (b) the monodisperse spray dryer.

production. This device allowed wide droplet spacing, thus preventing droplet–droplet interactions and disruption of the macroscopic fluid flow. Production frequencies on the order of 100 Hz were selected for this study. Under these conditions experiments were conducted in a well controlled gas phase similar to single droplet experiments, with the additional benefits of realistic droplet sizes and millisecond timescales.

The droplets were injected into a glass tube containing a laminar gas flow of controlled temperature, velocity, and relative humidity. The droplets were sized at different distances from the point of injection by analyzing the phase function of the elastical scattering (van de Hulst, 1981), which was generated by a focused probe laser beam (tunable diode laser, TC-30, SDL Inc., San Jose, CA, USA). The distance the droplets traveled as a function of time was measured using a second laser beam (diode laser, 635 nm, # 31-0334, Coherent Inc., Santa Clara, CA, USA) which was pulsed using the production frequency of the droplet generator. Due to the repeatable trajectories of the droplets a clear standing pattern was generated by the stroboscopic illumination. This pattern was analyzed to derive the relationship between time and distance. The dry particles were removed from the gas stream by a vacuum probe, which deposited the particles on membrane filters for subsequent scanning electron microscopy (SEM).

The droplet chain technique provides a highly controlled environment for droplet evaporation studies but is limited to production rates of much less than 1 mg of dried particles per hour. For diagnostic methods that require larger sample mass a second technique, schematically shown in Fig. 1b, was developed.

A modified vibrating orifice generator head (SBG-2000, Palas GmbH, Karlsruhe, Germany), based on the design introduced by Berglund and Liu (1973), was used as the atomizer in a custom benchtop spray dryer. The generator was fed with a syringe pump (#780-410, KD Scientific, Holliston, MA, USA) and produced monodisperse droplets in a size range from 20 to 100 μm at production frequencies of 10^5–10^6 Hz. The droplet chain was dispersed by a turbulent free jet with controlled gas temperature and mixed with independently controlled drying air. Drying was accomplished in a vertical glass chamber with a volume of 3200 cm^3. The dryer allowed sampling of droplets or particles at different positions with a vacuum probe. Particles were separated from the gas stream with a custom glass cyclone (MedImmune Inc., Mountain View, CA, USA) and collected in glass vials. The initial diameter, d_0, of the droplets was calculated using the mass balance:

$$d_0 = \sqrt[3]{\frac{6\dot{V}}{\pi f}}, \tag{10}$$

which is valid as long as the frequency, f, and the volume flow of the feed solution, $\dot{V}$, are chosen such that monodisperse operation is achieved. This was verified by the laminar crossflow method described by Ström (1969) and by measuring the width of the size distribution of the dried particles using a time-of-flight type particle sizing instrument (Model 3321, TSI Inc, Shoreview, MN, USA).

For aerosol testing, polydisperse powders were produced with a commercial benchtop spray dryer (#190, Büchi Labortechnik AG, Flawil, Switzerland), equipped with custom atomizers and cyclones (Nektar Therapeutics, San Carlos, CA, USA). Powders containing netilmicin sulfate, or gentamicin sulfate, were produced under the following conditions: liquid feed rate of 5 ml/min (1% w/w aqueous solutions), atomizing pressure of 414 kPa, controlled inlet drying gas temperature of 125 °C, and measured outlet temperature of 70 °C.

3.2. Methods

The droplet chain technique and the monodisperse spray dryer allow accurate determination of the initial droplet diameter, d_0. Hence, the particle density, ρ, of the produced dry particles can be derived according to the equation

$$\rho = c_f \cdot \left(\frac{d_0}{d_g}\right)^3, \tag{11}$$

where c_f denotes the solute concentration in the feed solution and d_g is the geometrical diameter of the dry particle.

Eq. (11) is exact for dry spheres. The geometric diameter of slightly non-spherical or rugose particles was determined manually or via image analysis software by averaging Feret's horizontal and vertical diameters, Feret (1930), for each particle in a group of monomorph particles. Feret's diameter, also known as caliper diameter, is the orthogonal distance between a pair of parallel tangents to the projection of the particle in a specific direction. Under the assumption that the particles are randomly oriented, the reported geometrical diameter is the orientation averaged Feret's diameter. This diameter provides the spherical reference volume for the calculation of the particle density. Because the reference volume includes internal and external voids in rugose particles, it is meaningful as an approximation for the aerodynamic behavior of the particles. This approach is not useful for particles with large aspect ratios such as rods or plates, which were not encountered in this study.

SEM was used to observe the morphology of the dried particles. Samples were prepared on aluminum SEM stubs. The mounted powders were then sputter-coated with gold–palladium in a Denton sputter-coater, achieving a coating thickness of approximately 15 nm. Most micrographs were taken with a Philips XL30 ESEM using a LaB6 source operated in high vacuum mode using an Everhart–Thornley detector to capture secondary electrons for the image composition.

Surface composition was determined by X-ray photoelectron spectroscopy (XPS) also known as electron spectroscopy for chemical analysis (ESCA). This technique probes the elemental surface composition by soft X-rays with a penetration depth of $\sim$ 5 nm. Samples for XPS were prepared using a glass plate (pre-cleaned with a 10% hydrofluoric acid solution) to press each powder sample onto a glass substrate that had been sandblasted to improve adhesion of the powder. A monochromatic Al X-ray source with a take-off angle of 45 ° was directed to a spot size of 2 × 3 mm on the sample. Spectra were collected with a Physical Electronics PHI 5000 Series Spectrometer. To convert the elemental concentrations to molecular concentrations of the components in the sample, a linear least squares model (JMP software, SAS Institute) was used to reconstruct the measured elemental atomic concentrations of the sample using the known elemental ratios of the components. The resulting concentrations were normalized to a total value of 100%.

Aerosol performance was characterized using an active dry powder inhaler, the Pulmonary Delivery System (PDS, Nektar Therapeutics, San Carlos, CA, USA) for powder dispersion and an eight stage cascade impactor (Series 20-800 Mark II, Thermo Scientific, Waltham, MA, USA) under controlled ambient conditions (21 °C and 40% RH). The PDS was operated with blister packages that contained 3 mg of powder. Two parameters were determined: the emitted dose, which is the mass of powder emitted from the device relative to the total mass in the blister package, and the fine particle mass < 3.3 μm. The emitted dose is a measure of device emptying efficiency. The fine particle mass is a measure of efficiency for deep lung delivery.

4. Results and discussion

4.1. Verification of experimental techniques

Several experiments were performed to verify the performance of the experimental apparatus and to test agreement between the numerical model and the experimental results. Fig. 2 shows the results of an evaporation rate measurement

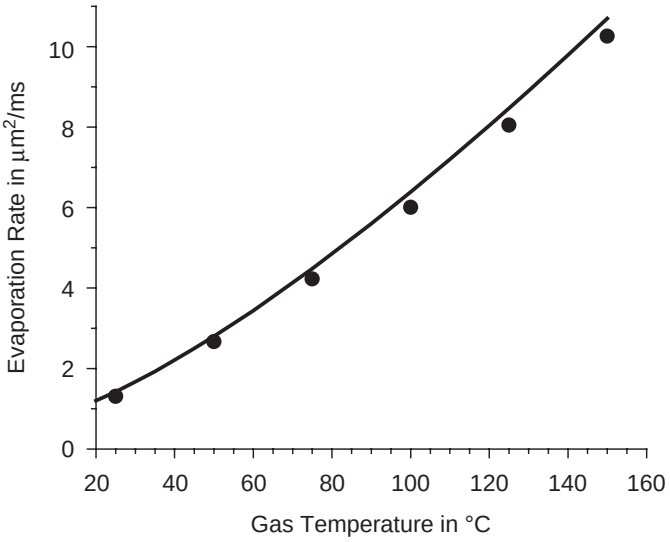

Fig. 2. Evaporation rates of pure water droplets measured by the droplet chain technique, shown as symbols, compared with the theoretical rates, plotted as closed line.

on pure water droplets in dry air. The symbols represent the experimental results. The water droplet diameter was determined as a function of distance from the point of injection by Mie scattering analysis. The distance the droplet had traveled was converted into elapsed time using the stroboscopic illumination provided by the experimental apparatus. Then the square of the diameter was plotted as a function of time. The slope of this plot yielded the evaporation rate. The closed line represents the analytical results of a simple steady-state evaporation model which describes the evaporation of a droplet in stagnant air and includes the effect of Stephan flow. The evaporation rate was calculated using Eq. (12) in which the steady-state droplet temperature, T_e, was determined iteratively by Eq. (13):

$$\kappa = \frac{8D\rho_g}{\rho_l} \ln\left(\frac{1 - Y_\infty}{1 - Y_s(T_e)}\right), \tag{12}$$

$$\frac{\Delta\hat{H}_v}{\hat{c}_p} = -\frac{(1 - Y_s(T_e))^{1/Le}(T_\infty - T_e)}{(1 - Y_\infty)^{1/Le} - (1 - Y_s(T_e))^{1/Le}}. \tag{13}$$

Derivation and nomenclature of the equations and expressions for the temperature-dependent material properties can be found in Appendix A.

The agreement between theory and experimental results is good, considering that the simple analytical model is limited to constant material properties in the gas phase. The results show that the droplet chain technique is suitable to study evaporation processes on a millisecond timescale with little interference from neighboring droplets or disturbance of the gas phase.

Fig. 3 shows the morphology of dried particles that were extracted from the flow tube of the droplet chain apparatus. The micrographs demonstrate that this technique is capable of producing nearly identical particles at various operating conditions. The particles shown consist of a glycoprotein with a molecular weight of 51 kDa. The top panel depicts particles dried at a low evaporation rate corresponding to dry air at a temperature of 25 °C, the middle panel shows the change in morphology when the evaporation rate was increased ($T = 50$ °C). The trend to more hollow particles was continued at a high drying temperature of 125 °C, shown in the bottom panel.

Fig. 4 shows trehalose particles generated by the monodisperse spray dryer. Typically, about 85% of the particles were monodisperse and showed a similar morphology. As expected, the level of control in this technique was lower but still adequate for accurate density measurements of the main population.

4.2. Low Peclet number particle formation

For $Pe \leqslant 1$, the diffusional velocity of the solute is faster or on the same order as the recession rate of the surface. Consequently, the radial concentration profile of the solute is predicted to be flat. If small Peclet numbers are coupled with

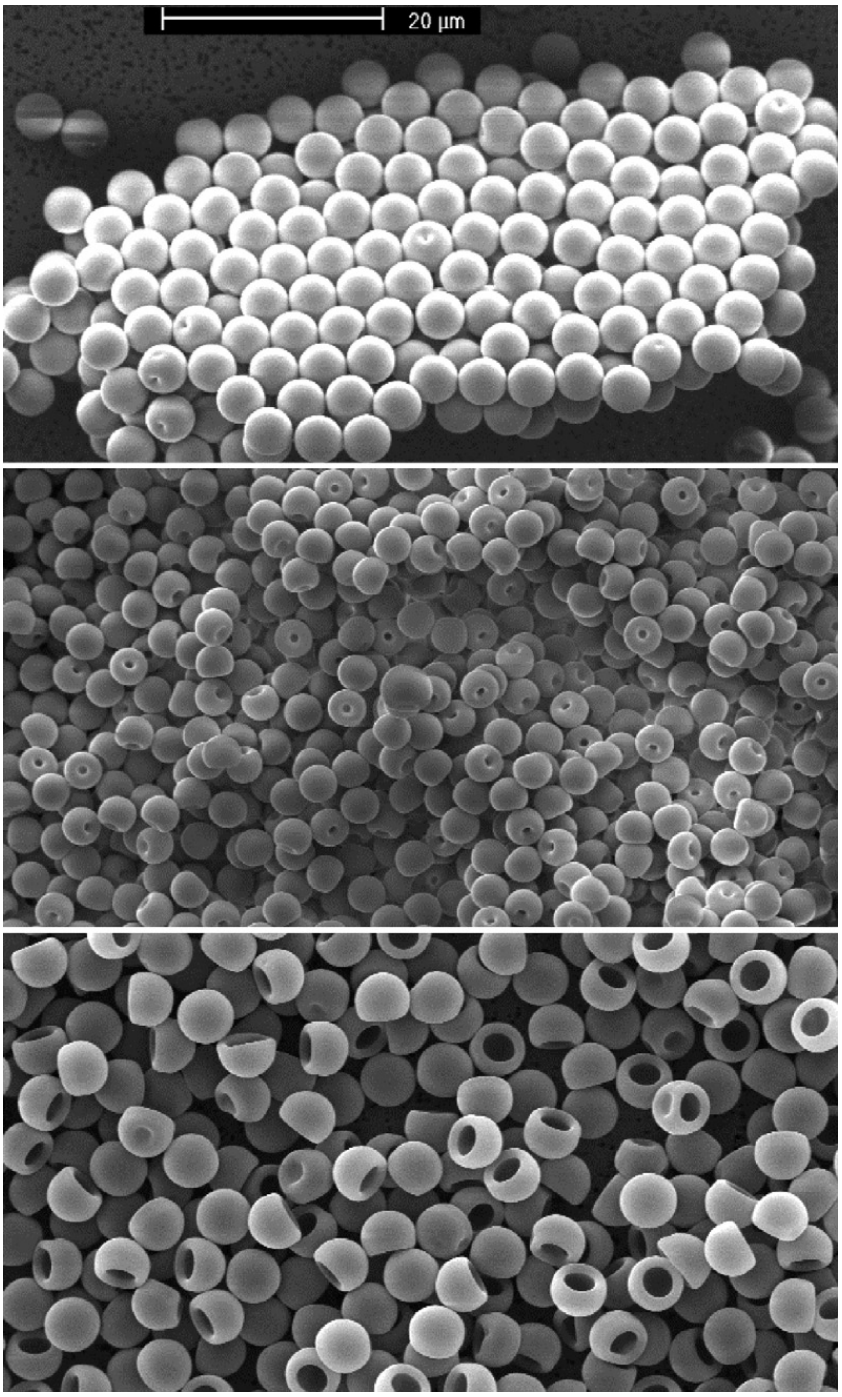

Fig. 3. Monodisperse, monomorph protein particles generated by the droplet chain technique. Drying gas temperatures from top to bottom: 25, 50, 125 °C.

a large solute solubility, precipitation is expected to appear late in the evaporation process and relatively homogeneously throughout the droplet. The resulting dry particles are expected to have little or no void space and a density close to the pycnometer density of the dried bulk material. This hypothesis was tested by drying trehalose solution droplets in the monodisperse spray dryer.

Fig. 4 shows typical morphologies of the resulting trehalose particles, which were dried with inlet conditions of 75 °C/ < 1% RH and outlet conditions of 46 °C/4.2% RH. This corresponds to evaporation rates of 4.1 and 1.7 μm^2/ms, respectively. With the diffusion coefficient for trehalose in water at the initial droplet concentration of 100 mg/ml, 5×10^{-10} m^2/s (Ekdavi-Sever, de Pablo, Feick, & von Meerwall, 2003), the initial Peclet number is in

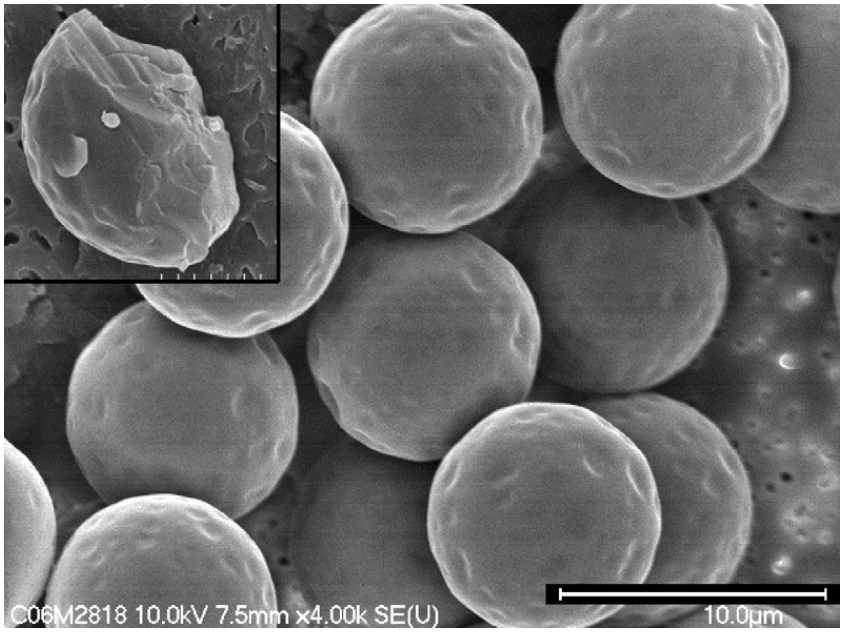

Fig. 4. Morphology of trehalose particles dried at a drying rate between 1.7 and 4.1 $\mu m^2/ms$. The insert shows an intentionally crushed particle.

the range of 0.44–1.0. An intentionally crushed particle, shown in the insert, reveals that these particles were indeed solid.

The particle density of trehalose particles was measured using different drying gas inlet temperatures from 55 to 100 °C. The results verify the findings of the electron microscopy. For all temperatures the particle density was in the range of 1.3–1.5 g/cm^3, close to the literature value for amorphous trehalose, 1.53 g/cm^3 (Zhang & Zografi, 2001), indicating solid particles in all cases.

Eq. (9) predicts that large Peclet numbers cause an enrichment of the solute at the surface which likely leads to shell or skin formation. Hence, even small molecules with high solubility such as saccharides are expected to form hollow particles if the evaporation rate is sufficiently high. This case was likely encountered in a study by Elversson, Millqvist-Fureby, Alderborn, and Elofsson (2003), where hollow lactose particles were formed using high drying gas temperatures of 200 °C at the inlet and 90 °C at the outlet, which corresponds to a Peclet number range of approximately 2–5. The case of large Peclet numbers is discussed in more detail in the next section.

4.3. Large Peclet number particle formation

Fig. 5 shows the densities of glycoprotein particles that were dried with the droplet chain technique at varying gas temperatures. Examples of morphologies for these particles are shown in Fig. 3. The droplets had an initial diameter of $\sim$ 16µm and the geometric diameter, also shown in Fig. 5, was kept between 4 and 6 µm. The Peclet number was calculated with a diffusion coefficient in water of 6×10^{-11} m^2/s, which was estimated using literature values for similar proteins. The density of the particles is significantly lower than the pycnometer density ($\sim$ 1.37 g/cm^3, Creighton, 1992) for all conditions, pointing to a large void space even in the particles that have no visible opening in the shell. The density drops further with increasing Peclet number which can also be seen in the increasing void size in Fig. 3.

The results shown in Fig. 6 shed light on the particle formation mechanism. The symbols represent measurements of the droplet size at different times of the evaporation. By plotting the square of the diameter against time it becomes clear that the evaporation closely follows the d^2-law for the first 50 ms. No diameter results are reported around 60 ms, because the measured phase function showed features that were unlike those expected from a sphere. The most likely explanation is that the droplets transitioned to dry particles at that time. After about 65 ms the phase function was usable again and the analysis yielded a diameter close to that measured by SEM on the dry particles. The closed line compares the experimental measurements with the results of the full numerical model. Very close agreement was achieved.

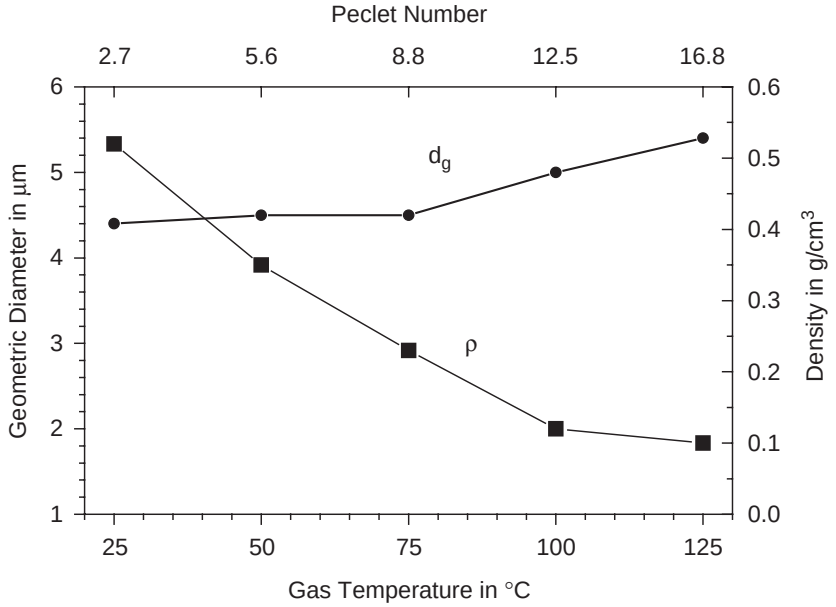

Fig. 5. Particle density, square symbols, of glycoprotein particles dried at different gas temperatures with the droplet chain technique. Also shown is the geometric diameter of the produced particles.

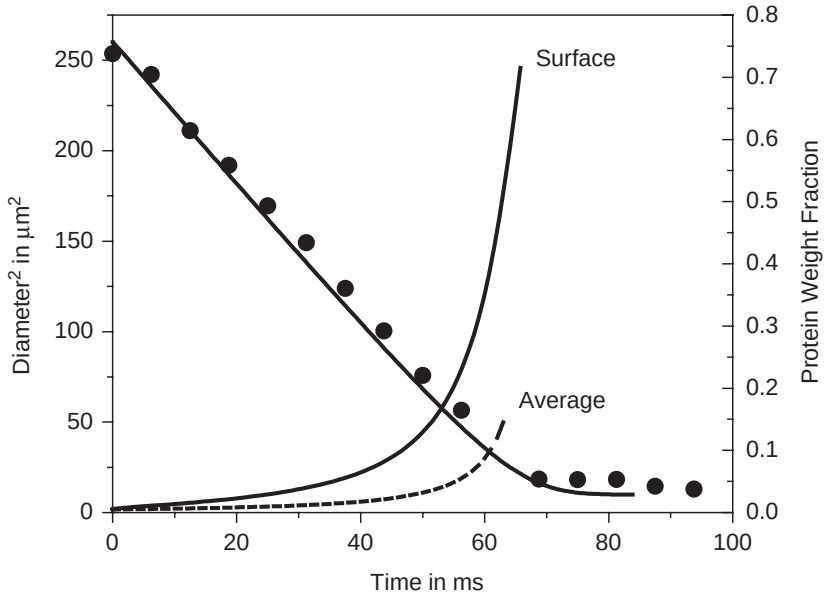

Fig. 6. Droplet and particle diameter measurements by Mie scattering, symbols, compared to results of the numerical model, closed line. Also shown are average, broken line, and surface protein weight fraction as a function of elapsed evaporation time.

The calculated local distribution of the protein in the droplet as a function of time is also shown in Fig. 6. The average protein weight fraction increases according to the loss of solvent, but the surface concentration of the protein increases much more quickly. The surface weight fraction reaches values close to one at a time when the light scattering data indicate solidification of the particle. This is strong evidence for a particle formation mechanism where the increasing viscosity of the surface enriched protein causes shell formation that prevents further shrinkage of the droplet.

The internal protein concentration profiles for a droplet with an initial diameter of 20 µm were calculated at various times in the evaporation process; the profiles are shown in Fig. 7. It is evident that the initially equal distribution of the protein changes gradually into a profile that shows strong surface enrichment. After about 300 ms the surface weight

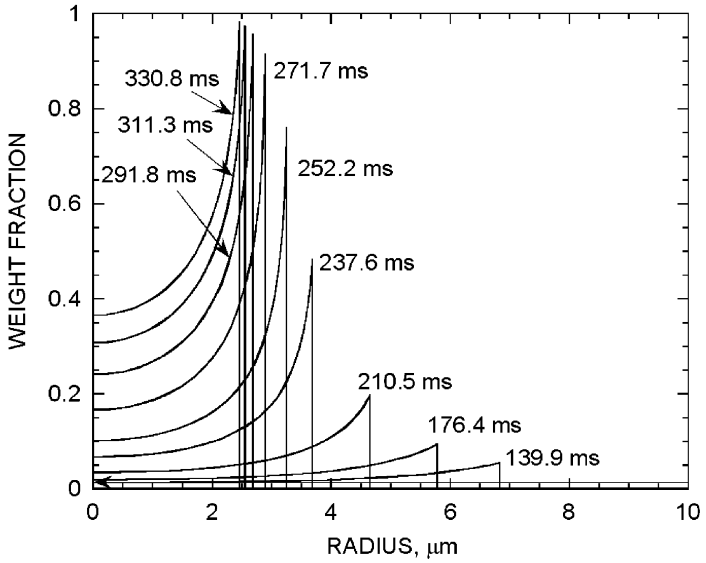

Fig. 7. Calculated radial distributions of a glycoprotein in an evaporating droplet. Initial droplet diameter, 20 μm; initial solute concentration, 10 mg/ml; initial Peclet number, 2.7. Variable material properties.

fraction reaches 1, and evaporation slows down significantly. The results of the numerical simulation become uncertain for high protein surface concentration, because material properties for these conditions are not available and need to be extrapolated with increasing uncertainty.

In summary, the results verify the hypothesized formation mechanism: a large Peclet number indicates that the recession of the surface is fast compared to the diffusional motion of the dissolved molecules. Therefore, the concentration of the solute increases sharply at the surface as the evaporation progresses. The high surface concentration leads to a local increase in viscosity with subsequent skin or shell formation. Once the skin is thick enough, it can maintain the shape of the particle. The remaining water is diffused through the shell or evaporates through openings in the shell. The hollow particle may finally collapse or wrinkle, depending on the thickness and mechanical properties of the skin.

4.4. Particle formation with changing Peclet numbers

Taken in isolation, the findings described above would indicate that small molecules dried at low Peclet numbers always produce solid particles. This is clearly not the case, as the wrinkled, low density particle shown in the insert in Fig. 8 demonstrates. This particle consists of Trileucine (L-Leucyl-L-Leucyl-L-Leucine), a small molecule dried at a Peclet number < 1.

Trileucine particles were dried using the droplet chain technique at Peclet numbers from 0.7 to 2 and had a consistently low particle density across the whole Peclet number range as shown in Fig. 8. The aspect ratio of some trileucine particles was not close to unity. To minimize the error in the density measurement the Feret diameters of at least 10 particles were averaged. A small systematic error may be present due to preferential orientation of the particles on the SEM substrate. Particles with three different diameters were produced, but differences in particle density were insignificant in the small diameter range studied in this experiment.

The results indicate that the initial Peclet number is not a controlling parameter in this case. The explanation for the observed behavior can be found in Fig. 9. As in Fig. 6 the measured evaporation data are compared to the results of the numerical model. The particle solidifies at about 90 ms, when the predicted surface concentration of the dissolved trileucine is still less than 25 mg/ml. This is clearly not close to a surface weight fraction of 1 as in the large Peclet number case described previously. However, because of the low solubility, c_{sol} of trileucine, 8 mg/ml, this concentration corresponds to a saturation, $S = c/c_{sol}$, of more than 2 at the surface. It is likely that the trileucine separates into a solid phase once it reaches supersaturation. The diffusion coefficient attributed to the phase separated domains is orders of magnitude smaller than that of the dissolved molecule. The corresponding Peclet number is much larger than 1, which is consistent with rapid surface accumulation of the phase separated material and explains the observed particle

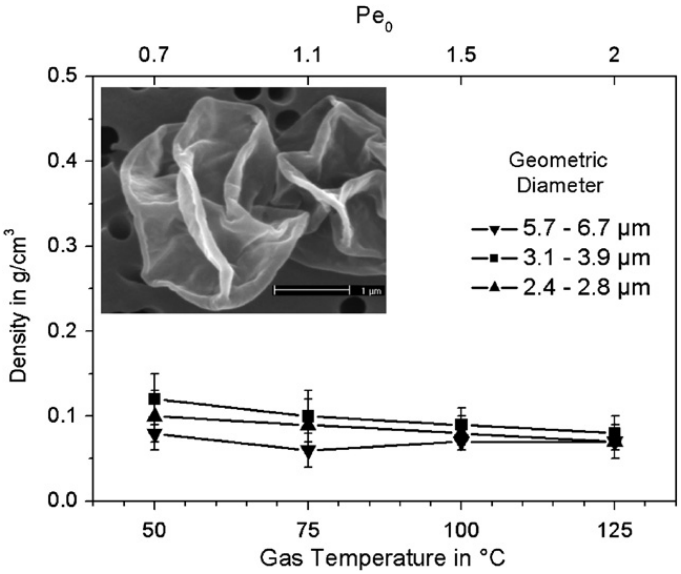

Fig. 8. Density of particles made from a low solubility, high surface activity molecule, trileucine. The initial droplet size was ~ 25 µm with varying solute concentrations yielding three geometric diameter ranges for the dry particles. The initial Peclet number was calculated with an estimated D of 5×10^{-10} m^2/s. The insert shows the morphology of trileucine particles dried at $Pe < 1$.

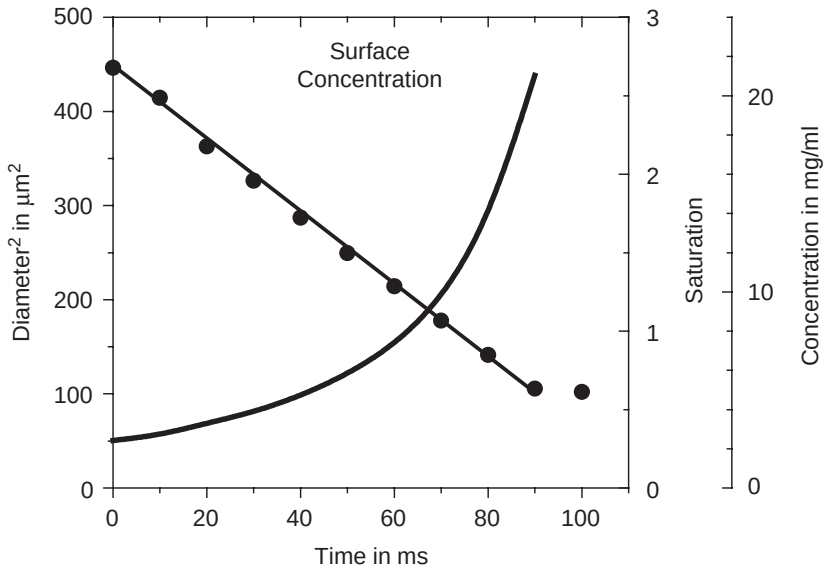

Fig. 9. Droplet and particle diameter measurements by Mie scattering, symbols, compared to results of the numerical model, closed line. Also shown is the trileucine surface concentration as a function of elapsed evaporation time.

morphology. Trileucine likely forms low density particles because of its low solubility which leads to phase separation and subsequent surface accumulation.

An alternative hypothesis is based on the high surface activity of trileucine. Surface active molecules may accumulate at the surface and form surface layers, which could play a role in the formation of a shell or skin. To test this hypothesis a dipetide, L-tyrosyl-L-isoleucine, was dried. This molecule has a solubility similar to that of trileucine, but is not surface active.

The results are shown in Fig. 10. This molecule also forms low density particles whose density is only weakly dependent on the Peclet number. This indicates that high surface activity is not a necessary condition for the formation of low density particles. It appears likely that surface activity is a parameter that influences the kinetics of phase

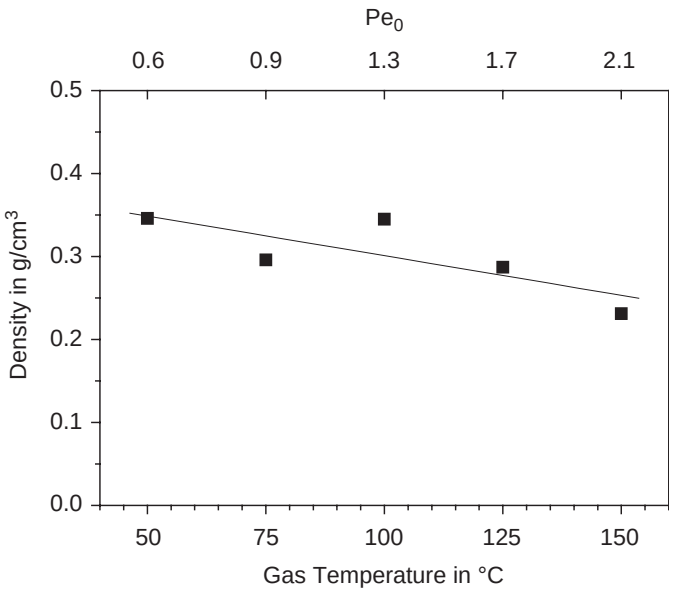

Fig. 10. Density of particles made from a low solubility, low surface activity molecule, tyrosine–isoleucine. The initial Peclet number was calculated with an estimated D of $6 \times 10^{-10}\,\mathrm{m}^2/\mathrm{s}$.

separation. In particular the nucleation phase may be affected by the presence of an ordered surface layer. This may explain why the densities observed for the surface active molecule were significantly lower than those of the control without surface activity.

In summary, the two dimensionless parameters that were found to affect the particle formation process most clearly were the Peclet number and the saturation of the solute. The Peclet number describes surface accumulation due to differences in the diffusional motion of the solute and the surface recession rate. The saturation correlates to the tendency of the solute to precipitate. These parameters do not describe the process completely; many important mechanisms such as nucleation, crystal growth rate, or buckling or crumpling of the shell are not captured. Nevertheless, the description of the process in the context of Pe and S allows prediction of radial concentration profiles in droplets which are about to solidify. These profiles should correlate to the internal distribution of components in multicomponent dry particles. Thus a rational approach to particle design becomes feasible, as shown in the next section.

4.5. Particle engineering

Two antibiotics were spray dried to produce powders for pulmonary administration. Gentamicin and netilmicin belong to the aminoglycoside family and are small molecules with similar molecular weights of 477.6 and 475.6 g/mol, respectively. The sulfate salts of the antibiotics are freely soluble in water. Both dried antibiotics had a similar morphology, smooth and dimpled particles with an intermediate density. Netilmicin sulfate particles are shown in the left panel of Fig. 11. To assess the aerosol performance of the powders, the emitted dose and the fine particle mass were determined as described in Section 3.2. The data in Fig. 12 and Table 1 show that the powder consisting of pure antibiotics had poor aerosol performance, likely because of low dispersibility of the particles.

Shekunov, Feeley, Chow, Tong, and York (2003) and Edwards et al. (2002) have pointed out that dispersibility can be improved by reducing particle density and inter-particle forces. Chew and Chan (2001) have further shown that particles with high rugosity disperse better than smooth particles. Therefore, the strategy to improve the aerosol performance of the powders was to replace antibiotic on the surface and to create a hollow, low density particle with a wrinkled morphology. To achieve this, trileucine was increasingly added to the formulation. According to the mechanism discussed above, at sufficient initial saturation, the trileucine was expected to precipitate sooner than the antibiotic, form a shell due to the increased Peclet number, and produce a low density wrinkled particle with similar morphology to the pure trileucine shown in Fig. 8.

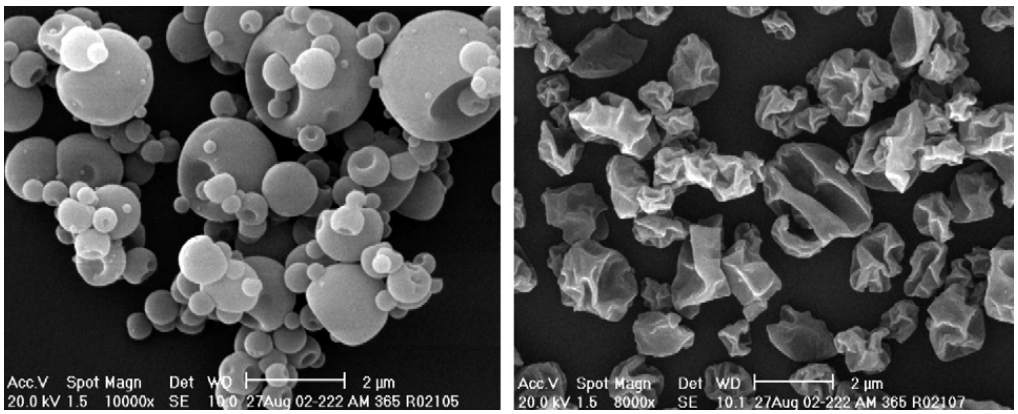

Fig. 11. Morphology of an antibiotic formulation with and without trileucine. Left panel: 100% netilmicin sulfate; right panel: 85% gentamicin sulfate, 15% trileucine.

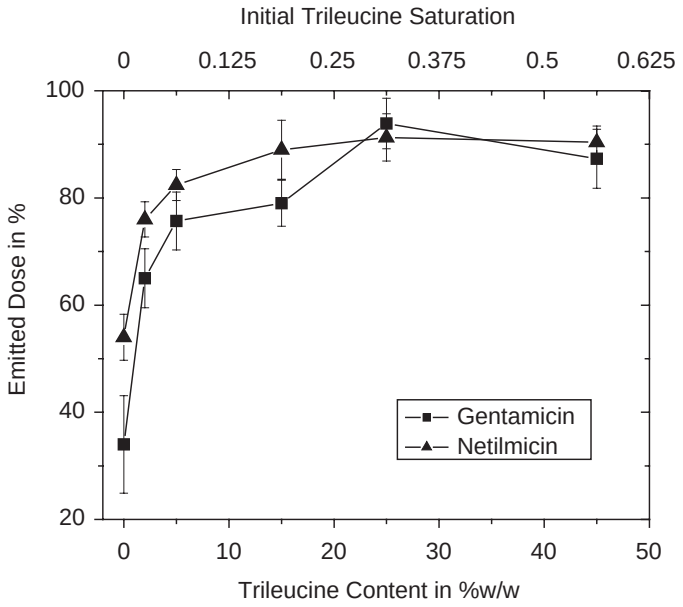

Fig. 12. Emitted dose of powder formulations of antibiotics with different trileucine content in the formulation. Formulation concentration was 10 mg/ml in all cases.

Table 1
Trileucine surface concentration by ESCA and fine particle mass < 3.3 µm as a function of trileucine content in the formulation

Trileucine content in the formulation	Trileucine surface concentration	Fine particle mass < 3.3 µm
Netilmicin		
0	–	28.5
2%	–	48.8
15%	56%	62.4
Gentamicin		
0	–	26.5%
2%	20%	46.8%
15%	45%	49.3%

Fig. 11 shows that this goal was achieved at a trileucine content in the formulation of 15%, corresponding to an initial trileucine saturation of 0.19. Increasing the initial trileucine saturation resulted in a gradual shift in morphology: smooth antibiotic particles started to resemble the rugose trileucine particles as trileucine was added. Further details are published elsewhere (Lechuga-Ballesteros et al., 2007).

ESCA measurements were performed to verify the trileucine surface enrichment. As shown in Table 1, at a trileucine content of 15% the trileucine mass fraction on the surface was more than three times that of the average mass fraction, which is in agreement with the postulated formation mechanism. At a trileucine content of 2%, the surface was enriched by an even larger factor of 10, while the morphology remained unchanged from that of the pure antibiotics (results not shown). This cannot be explained by a different mobility of the formulation components. It is likely that the observed surface enrichment is due to the high surface activity of trileucine. Because of its high diffusivity, the trileucine can diffuse toward the surface to form a surface layer on a shorter timescale than the lifetime of the droplet. Hence, at low trileucine contents the particles are expected to be homogeneous except for a thin coating of trileucine on the surface that is not rigid enough to form a shell capable of maintaining the shape of the particle.

The results in Fig. 12 and Table 1 show that the goal of improving the aerosol performance of the powder was achieved by redesigning the particle. An increase in emitted dose and fine particle mass was evident even at low trileucine concentrations. Most likely, the trileucine surface coverage reduced the inter-particle forces. Further dispersibility improvements were achieved at higher trileucine concentrations, where the benefits of a lower density and higher rugosity were added.

5. Conclusions

Many aspects of the particle formation process in spray drying are controlled by the relationship between surface recession and diffusion of the solutes. The mobility of the components changes during the evaporation process due to increasing solution viscosity or precipitation events. The details of the precipitation mechanisms are still difficult to describe, because nucleation and crystal growth processes are rather inaccessible experimentally and a theoretical description is hindered by a lack of material properties in supersaturated solutions. However, the steady-state evaporation process up to the point of particle solidification can be successfully studied both experimentally and theoretically as shown in this paper. Radial de-mixing of components can be understood and predicted in the context of dimensionless numbers, the Peclet number and the initial saturation of the solutes. Knowledge of the radial distribution of the components immediately prior to solidification in combination with empirical studies on single component particles allows prediction of the morphology of multi-component particles. Improved understanding of the particle formation process has lead to the successful design of structured microparticles with functional layers.

Acknowledgments

We would like to thank all our collaborators at the companies and institutions involved in this work, in particular, Mei-Chang Kuo, Danforth P. Miller, and Vathana Tep at Nektar Therapeutics, James Ivey at Medimmune, Inc. and Christopher I. Grainger at Kings College, London.

Appendix A. Calculation of the steady-state evaporation rate

The steady-state evaporation of a droplet in an infinite, uniform, stagnant gas was described by Fuchs (1959):

$$r^2 = r_0^2 - 2D\frac{\rho_g}{\rho_l}\ln\left(\frac{1-Y_\infty}{1-Y_s}\right)t. \tag{A.1}$$

(For nomenclature, see Table A1) This expression includes Stefan flow and assumes that the evaporation process can be described in the continuum regime, and that the diffusional flux is solely driven by a concentration gradient. The gas phase is limited to two components without chemical reactions, the solvent vapor and the drying gas, which are assumed to behave as an ideal gas mixture. The problem is described using a one-dimensional radial coordinate, assuming spherical symmetry. In this simplified description the material properties may not change with the radial coordinate. The stagnant gas phase condition includes the assumption that the solubility of the drying gas in the droplet and also the motion of the phase boundary are negligible.

Table A1
Nomenclature

c_p	Specific heat capacity of the solvent vapor
D	Diffusion coefficient of the solvent in the drying gas
$\Delta\hat{H}_v$	Standard enthalpy change of vaporization
Le	Lewis number
$\dot{m}$	Mass flux of solvent vapor
r	Droplet radius
r_0	Initial droplet radius
t	Time
T_s	Temperature at the droplet surface
T_∞	Temperature far away from the droplet
Y_∞	Mass fraction of the solvent vapor far away from the droplet
Y_s	Mass fraction of the solvent vapor at the droplet surface
κ	Evaporation rate
ρ_g	Density of the gas
ρ_l	Density of the liquid droplet
λ_g	Heat conductivity in the gas
Q_g	Energy flux in the gas

Eq. (A.1) only becomes useful when the partial pressure of the solvent at the droplet surface can be determined, i.e. the droplet temperature is known. The droplet temperature at steady state is determined by a balance of the energy necessary for the evaporation of the solvent and the net energy transported to the droplet through the gas.

The energy transport in the gas is determined by heat conduction and the energy necessary to heat the solvent vapor to the temperature of the gas mixture:

$$Q_g = \dot{m}\hat{c}_p(T - T_s) - 4\pi r^2 \lambda_g \frac{\partial T}{\partial r}. \tag{A.2}$$

Integration yields

$$\dot{m}\hat{c}_p = 4\pi r_s \lambda_g \ln\left(1 - \frac{\dot{m}\hat{c}_p(T_\infty - T_s)}{Q_g}\right). \tag{A.3}$$

Eq. (A.1) is based on the expression

$$\dot{m} = 4\pi r_s \rho_g D \ln\left(\frac{1 - Y_\infty}{1 - Y_s}\right), \tag{A.4}$$

which equated with (A.3) yields

$$\hat{c}_p \rho_g D \ln\left(\frac{1 - Y_\infty}{1 - Y_s}\right) = \lambda_g \ln\left(1 - \frac{\dot{m}\hat{c}_p\,(T_\infty - T_s)}{Q_g}\right).$$

After exponentiation and introduction of the Lewis number we find

$$1 - \frac{\dot{m}\hat{c}_p(T_\infty - T_s)}{Q_g} = \left(\frac{1 - Y_\infty}{1 - Y_s}\right)^{1/Le}, \quad Le = \frac{\lambda_g}{\hat{c}_p \rho_g D},$$

which can be rearranged as

$$\frac{Q_g}{\dot{m}\hat{c}_p} = -\frac{(1 - Y_s)^{1/Le} \cdot (T_\infty - T_s)}{(1 - Y_\infty)^{1/Le} - (1 - Y_s)^{1/Le}}. \tag{A.5}$$

The energy necessary to provide for the enthalpy change of vaporization at steady state is equal to the energy provided by the gas phase

$$Q_g = \dot{m}\Delta\hat{H}_v, \tag{A.6}$$

which substituted into Eq. (A.5) yields the desired expression for the temperature of the droplet undergoing steady-state evaporation:

$$\frac{\Delta\hat{H}_v}{\hat{c}_p} = -\frac{(1 - Y_s(T_e))^{1/Le} \cdot (T_\infty - T_e)}{(1 - Y_\infty)^{1/Le} - (1 - Y_s(T_e))^{1/Le}}. \tag{A.7}$$

This expression can be used to determine T_e iteratively, using the Clausius–Clapeyron relation to find the mass fraction of solvent.

From Eq. (A.1) the evaporation rate according to Eq. (3) follows as

$$\kappa = 8D\frac{\rho_g}{\rho_l}\ln\left(\frac{1 - Y_\infty}{1 - Y_s(T_e)}\right). \tag{A.8}$$

The material properties in the gas phase are assumed to be constant in the analysis above. This approximation is poor for high gas temperatures where the surface temperature of the droplet is much lower than the gas temperature at infinite distance from the droplet. Material properties that depend on the temperature and composition of the gas phase such as diffusion coefficient, density, and heat conductivity must be evaluated at a suitable reference condition to minimize the error introduced by this simplification (Miller, Harstad, & Bellan, 1998). Fuchs (1959) recommended the use of a geometric mean temperature for this purpose. Alternatively, the use of a $\frac{1}{3}$ rule has been proposed by Hubbard, Denny, and Mills (1975), where the material properties are evaluated at a temperature and water vapor mass fraction that is calculated by adding a third of the difference between surface and infinite distance conditions to the surface condition. Both evaluation schemes were tried and the $\frac{1}{3}$ rule lead to a closer agreement between experiment and theory. The result in Fig. 2 was calculated using the $\frac{1}{3}$ rule.

Diffusion coefficients were calculated using the reference equation given by Marrero and Mason (1972):

$$D = 1.87 \times 10^{-10}\,\mathrm{m^2\,s^{-1}} \times T^{2.072} \quad \text{with } T \text{ in Kelvin.}$$

The vapor pressure was calculated fitting an Antoine equation to the vapor pressure data tabulated in the *CRC handbook of chemistry and physics* (2002).

$$\log P_{sat} = A - \frac{B}{T + C}, \quad A = 10.113, \quad B = 1685.6, \quad C = -43.154, \quad T \text{ in } K, \quad P \text{ in Pa.}$$

The fit deviates from the tabulated data by less than 0.5% in the range of 0–200 °C.

Ideal gas law was used to calculate the gas density of moist air at the reference condition. The liquid water density and the specific heat capacity of the air are only weak functions of temperature. Polynomial fits to the data tabulated in the CRC Handbook were used in the iteration. The heat conductivity at the reference condition was calculated using a linear fit to the data tabulated in *Dubbel*, *Taschenbuch für den Maschinenbau* (1983). The enthalpy change of vaporization also varies nearly linearly with temperature in the range of 0–100 °C; tabulated data from Sabbah et al. (1999) was used to calculate the enthalpy change of vaporization at the droplet equilibrium temperature.

Appendix B. Governing equation for the numerical model

The mass balance for component i in the droplet and in the gas phase was described by

$$\rho\frac{\partial Y_i}{\partial t} + \rho v\frac{\partial Y_i}{\partial r} = \frac{1}{r^2}\frac{\partial}{\partial r}\left(r^2\rho D_i\frac{\partial Y_i}{\partial r}\right). \tag{B.1}$$

The first term describes transient accumulation of component i, the second term represents the convected mass flux and the third term the diffusive mass flux. One fewer mass balance than the total number of components was used. The mass fraction of the last species was found using the condition that the sum of all mass fractions must equal 1. The radial velocity for the convective transport term was found from the overall equation of continuity:

$$\frac{\partial\rho}{\partial t} + \frac{1}{r^2}\frac{\partial}{\partial r}(r^2\rho v) = 0. \tag{B.2}$$

The total density was found by using an additive equation of state in the liquid phase and ideal gas law in the gas phase.

The boundary conditions for the component mass balances were:

- No mass flux and zero velocity at the center of the sphere.
- Convected and diffusive mass flow at the droplet surface must be equal in the liquid and the gas phase. The chemical activities of the volatile components in both phases must also match at the surface.
- Zero velocity far from the sphere, and the concentrations of the gas phase components can either be constant or can vary with time defined by an external function.

The energy balance in the gas phase was modeled by

$$\rho c_p \frac{\partial T}{\partial t} + \rho c_p v \frac{\partial T}{\partial r} = \frac{1}{r^2}\frac{\partial}{\partial r}\left(r^2 \lambda \frac{\partial T}{\partial r}\right) + \frac{1}{r^2}\frac{\partial}{\partial r}\left(r^2 \rho \sum_i \hat{H}_i D_{i,\mathrm{mix}} \frac{\partial Y_i}{\partial r}\right). \tag{B.3}$$

The first term describes the change of temperature with time, the second term describes convective heat transport, the third term represents Fourier's law to describe heat conduction, and the last term considers diffusive enthalpy transport.

The temperature of the droplet was assumed to be uniform. It was determined by using the boundary condition that the energy transported from the gas phase to the surface of the droplet by conduction and diffusion must equal the change in latent heat plus the enthalpy needed for the phase change. Further boundary conditions were matching gas and liquid temperatures at the surface of the droplet and either constant temperature far from the sphere or alternatively a time-dependent temperature far from the droplet defined by an external function.

References

Adhikari, B., Howes, T., Bhandari, B. R., & Truong, V. (2000). Experimental studies and kinetics of single drop drying and their relevance in drying of sugar-rich foods: A review. *International Journal of Food Properties*, *3*, 323–351.

Alexander, K., & King, C. J. (1985). Factors governing surface morphology of spray-dried amorphous substances. *Drying Technology*, *3*, 321–348.

Anders, K., Roth, N., & Frohn, A. (1992). Operation characteristics of vibrating-orifice generators: The coherence length. *Particle & Particle Systems Characterization*, *9*, 40–43.

Berglund, R. N., & Liu, B. Y. H. (1973). Generation of monodisperse aerosol standards. *Environmental Science & Technology*, *7*, 147–153.

Beitz, W., & Küttner, K.-H. (Eds.), *Dubbel*, *Taschenbuch für den Maschinenbau* (1983). Berlin: Springer.

Charlesworth, D. H., & Marshall, W. R., Jr. (1960). Evaporation from drops containing dissolved solids. *AIChE Journal*, *6*, 9–23.

Chen, X. D., & Lin, S. X. Q. (2004). Air drying of milk droplet under constant and time-dependent conditions. *AIChE Journal*, *51*, 1790–1799.

Chew, N. Y. K., & Chan, H.-K. (2001). Use of solid corrugated particles to enhance powder performance. *Pharmaceutical Research*, *18*, 1570–1577.

Creighton, T. E. (1992). *Proteins: Structures and molecular properties*. New York: W.H. Freeman.

Davis, E. J. (1983). Transport phenomena with single aerosol particles. *Aerosol Science and Technology*, *2*, 121–144.

Devarakonda, V., & Ray, A. K. (2003). Effect of inter-particle interactions on evaporation of droplets in a linear array. *Journal of Aerosol Science*, *34*, 837–857.

Edwards, D. A., Caponetti, G., Hrkach, J., Lotan, N., Hanes, J., Ben-Jebria, A. et al. (2002). Aerodynamically light particles for pulmonary drug delivery. *USA Patent*: 6,399,102.

Ekdavi-Sever, N., de Pablo, J. J., Feick, E., & von Meerwall, E. (2003). Diffusion of sucrose and alpha, alpha-trehalose in aqueous solutions. *Journal of Physical Chemistry A*, *107*, 936–943.

El Golli, S., Bricard, J., Turpin, P.-Y., & Treiner, C. (1974). The evaporation of saline droplets. *Journal of Aerosol Science*, *5*, 273–292.

El-Sayed, T. M., Wallack, D. A., & King, C. J. (1990). Changes in particle morphology during drying of drops of carbohydrate solutions and food liquids. 1. Effects of composition and drying conditions. *Industrial & Engineering Chemistry Research*, *29*, 2346–2354.

Elversson, J. E., & Millqvist-Fureby, A. (2005). Particle size and density in spray drying—effects of carbohydrate properties. *Journal of Pharmaceutical Sciences*, *94*, 2049–2060.

Elversson, J. E., Millqvist-Fureby, A., Alderborn, G., & Elofsson, U. (2003). Droplet and particle size relationship and shell thickness of inhalable lactose particles during spray drying. *Journal of Pharmaceutical Sciences*, *92*, 900–910.

Fäldt, P., & Bergenståhl, B. (1994). The surface composition of spray-dried protein–lactose powders. *Colloids and Surfaces A: Physicochemical and Engineering Aspects*, *90*, 183–190.

Feret, L. R. (1930). La Grosseur des Grains des Matières Pulvérulentes. *Premières Communications de la Nouvelle Association Internationale pour l'Essai des Matériaux. Groupe D.* Zürich, NAIEM.

Fuchs, N. A. (1959). *Evaporation and droplet growth in gaseous media*. London: Pergamon Press.

Greenwald, C. G., & King, C. J. (1982). The mechanism of particle expansion in spray drying of foods. *Food Process Engineering*, *78*, 101–110.

Hubbard, G. L., Denny, V. E., & Mills, A. F. (1975). Droplet evaporation: Effects of transients and variable properties. *International Journal of Heat and Mass Transfer*, *18*, 1003–1008.

Kreidenweis, S. M., Flagan, R. C., & Seinfeld, J. H. (1987). Evaporation and growth of multicomponent aerosols laboratory applications. *Aerosol Science and Technology*, *6*, 1–14.

Kuo, M.-C., & Lechuga-Ballesteros, D. (2003). Dry powder compositions having improved dispersivity. *USA Patent*: 6,518,239.

Law, C. K. (1982). Recent advances in droplet vaporization and combustion. *Progress in Energy and Combustion Science*, *8*, 171–201.

Lechuga-Ballesteros, D., Charan, C., Stults, C., Stevenson, C.L., Miller, D.P., Vehring, R., et al. (2007). Trileucine improves dispersibility, aerosol performance and stability of spray-dried powders for inhalation. *Journal of Pharmaceutical Sciences*, accepted for publication.

Leong, K. H. (1987). Morphological control of particles generated from the evaporation of solution droplets: Theoretical considerations. *Journal of Aerosol Science*, *18*, 511–524.

Lide, D. R. (Ed.), *CRC handbook of chemistry and physics* (2002). Boca Raton, FL: CRC Press.

Lin, J.-C., & Gentry, J. W. (2003). Spray drying drop morphology: Experimental study. *Aerosol Science and Technology*, *37*, 15–32.

Lin, S. X. Q., & Chen, X. D. (2002). Improving the glass-filament method for accurate measurement of drying kinetics of liquid droplets. *Chemical Engineering Research and Design*, *80*, 401–410.

Lin, S. X. Q., & Chen, X. D. (2004). Changes in milk droplet diameter during drying under constant drying conditions investigated using the glass-filament method. *Food and Bioproducts Processing*, *82*, 213–218.

Maa, Y.-F., Costantino, H. R., Nguyen, P.-A., & Hsu, C. C. (1997). The effect of operating and formulation variables on the morphology of spray-dried protein particles. *Pharmaceutical Development and Technology*, *2*, 213–223.

Marrero, T. R., & Mason, E. A. (1972). Gaseous diffusion coefficients. *Journal of Physical and Chemical Reference Data*, *1*, 3–118.

Masters, K. (1972). *Spray drying—an introduction to principles, operational practice and applications*. London: Leonard Hill Books.

Miller, R. S., Harstad, K., & Bellan, J. (1998). Evaluation of equilibrium and non-equilibrium evaporation models for many-droplet gas–liquid flow simulations. *International Journal of Multiphase Flow*, *24*, 1025–1055.

Newbold, F. R., & Amundson, N. R. (1973). A model for evaporation of a multicomponent droplet. *AIChE Journal*, *19*, 22–30.

Platz, R. M., Patton, J. S., Foster, L., & Eljamal, M. (2002). Methods of spray-drying a drug and a hydrophobic amino acid. *USA Patent*: 6,372,258.

Raula, J., Eerikäinen, H., & Kauppinen, E. I. (2004). Influence of the solvent composition on the aerosol synthesis of pharmaceutical polymer nanoparticles. *International Journal of Pharmaceutics*, *284*, 13–21.

Sabbah, R., Xu-wu, A., Chickos, J. S., Planas Leitao, M. L., Roux, M. V., & Torres, L. A. (1999). Reference materials for calorimetry and differential thermal analysis. *Thermochimica Acta*, *31*, 93–204.

Shekunov, B. Y., Feeley, J. C., Chow, A. H. L., Tong, H. H. Y., & York, P. (2003). Aerosolisation behaviour of micronised and supercritically-processed powders. *Journal of Aerosol Science*, *34*, 553–568.

Ström, L. (1969). The generation of monodisperse aerosols by means of a disintegrated jet of liquid. *Review of Scientific Instruments*, *40*, 778–782.

Sugiyama, Y., Larsen, R. J., Kim, J.-W., & Weitz, D. A. (2006). Buckling and crumpling of drying droplets of colloid-polymer suspensions. *Langmuir*, *22*, 6024–6030.

Sunkel, J. M., & King, C. J. (1993). Influence of the development of particle morphology upon rates of loss of volatile solutes during drying of drops. *Industrial & Engineering Chemistry Research*, *32*, 2357–2364.

Tsapis, N., Bennett, D., Jackson, B., Weitz, D. A., & Edwards, D. A. (2002). Trojan particles: Large porous carriers of nanoparticles for drug delivery. *Proceedings of the National Academy of Sciences of the United States of America*, *99*, 12001–12005.

Tsapis, N., Dufresne, E. R., Sinha, S. S., Riera, C. S., Hutchinson, J. W., Mahadevan, L. et al. (2005). Onset of buckling in drying droplets of colloidal suspensions. *Physical Review Letters*, *94*, 018302.

van de Hulst, H. C. (1981). *Light scattering by small particles*. New York: Dover Publications.

Vehring, R., & Schweiger, G. (1991). Raman scattering on liquid aerosol particles: Concentration measurements on droplet chains. *Journal of Aerosol Science*, *22*, S399–S402.

Wallack, D. A., El-Sayed, T. M., & King, C. J. (1990). Changes in particle morphology during drying of drops of carbohydrate solutions and food liquids. 2. Effects on drying rate. *Industrial & Engineering Chemistry Research*, *29*, 2354–2357.

Walton, D. E., & Mumford, C. J. (1999). The morphology of spray-dried particles. The effect of process variables upon the morphology of spray-dried particles. *Transactions of the Institution of Chemical Engineers*, *77A*, 442–460.

Weers, J. G., Schutt, E. G., Dellamary, L. A., Tarara, T. E., & Kabalnov, A. (2001). Stabilized preparations for use in metered dose inhalers. *USA Patent*: 6,309,623.

Zhang, J., & Zografi, G. (2001). Water vapor absorption into amorphous sucrose-poly(vinyl pyrrolidone) and trehalose-poly(vinyl pyrrolidone) mixtures. *Journal of Pharmaceutical Sciences*, *90*, 1375–1385.